Chinese Chemical Letters 34 (2023) 107776

Contents lists available at ScienceDirect

Chinese Chemical Letters

journal homepage: www.elsevier.com/locate/cclet

High-entropy perovskite oxide $BaCo_{0.2}Fe_{0.2}Zr_{0.2}Sn_{0.2}Pr_{0.2}O_{3-\delta}$ with triple conduction for the air electrode of reversible protonic ceramic cells

Jiaxiang Sun, Rongzheng Ren*, Hualiang Yue, Wencan Cui, Gaige Wang, Chunming Xu, Jinshuo Qiao, Wang Sun, Kening Sun, Zhenhua Wang*

Beijing Key Laboratory for Chemical Power Source and Green Catalysis, School of Chemistry and Chemical Engineering, Beijing Institute of Technology, Beijing 100081, China

ARTICLE INFO

Article history:
Received 12 July 2022
Revised 7 August 2022
Accepted 22 August 2022
Available online 28 August 2022

Keywords:
High-entropy perovskite oxide
Triple-conducting oxide
Air electrode
Reversible protonic ceramic cells
Hydrogen production

ABSTRACT

Reversible protonic ceramic cells (RPCCs) show great potential as new-generation energy conversion and storage devices. However, the mature development of RPCCs is seriously hindered by the inactivity and poor stability of air electrodes exposed to concentrated vapor under operating conditions. Herein, we report a high-entropy air electrode with the composition $BaCo_{0.2}Fe_{0.2}Zr_{0.2}Sn_{0.2}Pr_{0.2}O_{3-\delta}$ (BCFZSP), which shows integrated electronic, protonic and oxygenic conduction in a single perovskite phase and excellent structural stability in concentrated steam. Such triple conduction can spread the electrochemically active sites of the air electrode to the overall electrode surface, thus optimizing the kinetics of the oxygen reduction and evolution reactions (0.448 Ω cm^2 of polarization resistance at 550 °C). As-prepared RPCCs with a BCFZSP air electrode at 600 °C achieved a peak power density of 0.68 W/cm^2 in fuel-cell mode and a current density of 0.92 A/cm^2 under a 1.3 V applied voltage in electrolysis mode. More importantly, the RPCCs demonstrate an encouragingly high stability during 120 h of reversible switching between the fuel-cell and electrolysis modes. Given their excellent performance, high-entropy perovskites can be promising electrode materials for RPCCs.

In today's sustainable energy economy, the use of intermittent wind-based and solar electricity generation has exploded, increasing the demand for efficient and reliable energy conversion and storage devices [1]. Reversible protonic ceramic cells (RPCCs) are the most promising developments among long-term and large-scale energy conversion and storage [2]. In the application of RPCCs, the chemical energy from hydrogen is converted into electrical energy when electricity is required and dry pressure hydrogen can be electrolyzed for storage from excess solar and wind-based electricity [3]. Owing to the unique property of proton hopping between adjacent oxygen atoms, RPCCs exhibit excellent proton conductivity, low activation energy (E_a) at intermediate temperatures (400–600 °C), and stable performance [4]. In electrolysis mode, dry pressurized hydrogen is continuously generated at the fuel electrode and then stored in an external pressure vessel. This process lowers the cost by removing the need for a fuel-separation device. In fuel-cell mode, hydrogen reacts at the anode while water is generated at the cathode, which reduces the dilution of fuel by water.

Although RPCCs offer distinct advantages, their large-scale commercial applications are limited by the unsatisfactory oxygen reduction reaction (ORR) and oxygen evolution reaction (OER) activity. These problems arise from lack of a suitable air electrode. Many RPCCs use mixed ionic and electronic conductor (MIEC) electrodes such as $Ba_{0.5}Sr_{0.5}Co_{0.8}Fe_{0.2}O_{3-\delta}$ (BSCF) and $La_{0.6}Sr_{0.4}Co_{0.2}Fe_{0.8}O_{3-\delta}$ (LSCF), which exhibit remarkable electrical conductivity and electrocatalytic activity [5]. However, MIECs in proton-conductive RPCCs are unsuitable for several reasons. First, because MIECs have poor water-absorption capacity, they cannot provide sufficient protons from the hydration reaction [4]. Second, the reactive sites are restricted to a narrow triple-phase boundary (TPB) between the electrode and electrolyte, which suppresses the ORR activity [6]. Third, MIEC electrodes decompose in a high vapor-concentration atmosphere thus destabilize the electrochemical performance [7].

To improve the proton conductivity and widen the TPB, air electrodes that can transport electrons (e^-), oxide ions (O^{2-}), and protons (H^+) are required. Such electrode materials, called triple-conducting oxides (TCOs), present more reac-

---

* Corresponding authors.

E-mail addresses: 7520200218@bit.edu.cn (R. Ren), wangzh@bit.edu.cn (Z. Wang).

https://doi.org/10.1016/j.cclet.2022.107776

tive active sites throughout the electrode surface that boost the ORR and OER activities [8]. Some composite electrodes with triple conductive properties have been reported recently, such as $PrBa_{0.8}Ca_{0.2}Co_2O_{5+\delta}$–$BaCoO_{3-\delta}$ [9], NiO nanoparticle-modified $Ba_{0.95}(Co_{0.4}Fe_{0.4}Zr_{0.1}Y_{0.1})_{0.95}Ni_{0.05}O_{3-\delta}$ [10], and so forth [11]. However, industrially fabricating composite cathodes are limited by a cumbersome process. Thus, more studies have focused on single-phase electrodes [12]. Compared to the composited electrode, single TCOs show definite chemical composition, which is more suitable for facile preparation and large-scale application. A series of classic single TCOs have been developed, including $PrBa_{0.5}Sr_{0.5}Co_{1.5}Fe_{0.5}O_{5+\delta}$ [13], $BaCo_{0.4}Fe_{0.4}Zr_{0.1}Y_{0.1}O_{3-\delta}$ (BCFZY) [14], and so forth [15]. In single TCOs, protons are mainly generated from the hydration of oxygen vacancies and external water. Thus, the design of single TCOs is challenged by the need for plentiful water uptake at the oxygen vacancies for copious proton production.

High-entropy oxides (HEOs) are advantaged by thermal stability and formation of oxygen defects. HEOs are single-phase oxides containing at least five different cations in equiatomic amounts [16]. Thus, the multi-functional requirements can be met by selecting the appropriate elements. HEOs possess thermodynamic stability due to high configuration enthalpy [16]. By virtue of their outstanding properties, HEOs have been widely applied in energy storage and conversion technologies. Liu *et al.* boosted the Cr-poisoning tolerance of the cathode in solid oxide fuel-cells (SOFCs) [17]. Liu *et al.* enhanced and stabilized the ORR performance in rechargeable metal–air batteries [18]. Wang *et al.* improved the oxygen evolution activity in effective OER catalysis [19]. However, to the best of our knowledge, HEOs with triple-conductive properties have not been reported in RPCCs. Therefore, a suitable design approach for air electrodes with high electrocatalytic performance and extraordinary stability is vital to RPCCs development.

Herein, $BaCo_{0.2}Fe_{0.2}Zr_{0.2}Sn_{0.2}Pr_{0.2}O_{3-\delta}$ (BCFZSP), a high-entropy perovskite oxide, was designed and employed as the electrode for RPCCs. And BCFZY such a classic TCO has been selected as the control sample to better analyze the triple conduction of BCFZSP. Compared with the BCFZY, BCFZSP presents a high proton diffusion coefficient. At 600 °C, the BCFZSP electrode with an approximately 8-µm-thick $BaZr_{0.4}Ce_{0.4}Y_{0.1}Yb_{0.1}O_{3-\delta}$ electrolyte achieved a peak power density of 677 mW/cm^2 in fuel-cell mode. In electrolysis mode, the current density reached 0.92 A/cm^2 at an applied voltage of 1.3 V. The eminent polarization resistance was 0.448 Ω cm^2 at 550 °C. More importantly, the full cell degraded minimally after 120 h operation and completely recovered with no performance degradation during 120 h switching cycles. Both the high ORR activity and excellent stability at low temperatures suggest that BCFZSP is a promising high-entropy electrode for RPCCs.

Energy dispersive X-ray spectroscopy (EDS) mapping showed that all the elements are uniformly distributed in BCFZSP sample (Fig. 1a), and the estimated atom ratio of Ba:Co:Fe:Zr:Sn:Pr matched well with the nominal value for BCFZSP (Table S1 in Supporting information). The X-ray diffraction (XRD) Rietveld refinement results suggest that the BCFZSP showed a single perovskite phase with a Pm-3 m space group and a cell parameter of $a = b = c = 4.183(5)$ Å (Fig. 1b and Table S2 in Supporting information). The estimated lattice fringe distance of 0.295 nm in high-resolution transmission electron microscopy (HR-TEM) matched well with the $(10\bar{1})$, $(01\bar{1})$, and $(\bar{1}10)$ facets along the [111] zone axis (Fig. 1c). The corresponding selected area electron diffraction (SAED) pattern also confirms this crystal plane alignment (Fig. 1d). All of these results indicated the B-site cations were completely dissolved into the lattice of HEOs without impure phases. X-ray photoelectron spectroscopy (XPS) results indicate that Co/Fe/Pr exhibite a mixed valence state (Co and Fe: +2/+3; Pr: +3/+4), while Zr and Sn cations show fixed valence state of +4 (Fig. S1 in Supporting information). Notably, the BCFZSP can maintain pure phase at a concentrated steam atmosphere with $p(H_2O)$ as high as 50% atm, suggesting its excellent structure stability (Fig. S2 in Supporting information).

In electrolysis mode, water molecules are adsorbed on the surface of oxygen electrode. The adsorption relies on the hydration reaction between oxygen vacancies and water molecules, thus generating proton defects (Figs. 2a and b). In fuel-cell mode, the water formed by the combination of proton defects and lattice oxygen that escapes from the lattice gap (Figs. 2b and c). Therefore, the interaction between H_2O and oxygen vacancy contribute greatly to the electrochemical performance of RPCCs. For evaluating this interaction, thermogravimetric analysis (TGA) was carried out (Fig. 2d). First, the samples were heated from the room temperature to 900 °C to form oxygen vacancies. Then the samples were cooled under dry and wet air ($p(H_2O) = 10\%$ atm) respectively to observe the adsorption behavior of oxygen and H_2O. A higher weight loss can be observed for BCFZY during the heating process, meaning more vacancies of BCFZY than BCFZSP. Given that the weight loss of perovskite oxides at evaluated temperature is closely related to the reduction of Fe/Co cations, the more vacancies in BCFZY is mainly ascribed to more Fe/Co content in BCFZY. During the cooling stage, the increase of mass in dry air is attributed to the absorption of oxygen (Eq. 1).

$$V_O^{\cdot\cdot} + \frac{1}{2}O_2 \rightarrow O_O^{\times} + 2h^{\cdot} \tag{1}$$

While cooling in the wet state, both the O_2 absorption and H_2O uptake can lead to the weight increase (Eq. 2).

$$V_O^{\cdot\cdot} + H_2O + O_O^{\times} \rightarrow 2OH_O^{\cdot} \tag{2}$$

Based on the weight difference under different cooling atmosphere, the proton concentration can be calculated [4]. It is interesting that more proton defects can be detected in BCFZSP (Fig. 2e), even though the oxygen vacancy concentration of BCFZSP is lower than that of BCFZY. Specifically, the proton concentration in BCFZSP at 500 °C and 10% atm $p(H_2O)$ was 6.92 mol%, *versus* 1.34 mol% in BCFZY. This result suggests that the water adsorption capacity of oxygen vacancy in BCFZSP is much stronger than that of BCFZY. TG relaxation technique with dry/wet atmosphere switching was further used to compare the hydration/dehydration capacity of BCFZSP and BCFZY (Fig. 2f). After a rapid change between dry and wet ($p(H_2O) = 10\%$ atm) atmosphere, a sharper weight change signal in BCFZSP reveals a better hydration and dehydration ability of BCFZSP. All these results emphasize that the high-entropy perovskite oxide shows enhanced hydration/dehydration ability.

Electrical conductivity relaxation (ECR) method was further carried out to quantify the triple conduction and water exchange process of the BCFZSP electrode. It should be noted that the ECR used here was performed on a fixed oxygen partial pressure ($p(O_2) = 21\%$) but a varied $p(H_2O)$. Once the pH_2O is increased, oxygen vacancies in perovskite will be occupied, the concentration of all carriers in TCOs, including the oxygen vacancies, holes ($h^{\cdot}$), and proton defects ($OH_O^{\cdot}$), can be redistributed (Fig. 3), hence forming concentration gradient. This mechanism offers a feasible path to uncover the triple conduction and water exchange process of the BCFZSP electrode.

Figs. 4a and b are ECR configurations of BCFZSP and $BaZr_{0.4}Ce_{0.4}Y_{0.1}Yb_{0.1}O_{3-\delta}$ (BZCYYb) when switching the atmosphere from dry to wet state at 600 °C. A nonmonotonic relaxation curve can be observed with $p(H_2O)$ suddenly increasing. The conductivity of two samples initially dropped and then raised to a new equilibrium. This nonmonotonic transformation was ascribed to hole redistribution during the hydration reaction. Because the electronic conductivity in TCOs is much higher than ionic conductivity, the conductivity change as function of $p(H_2O)$ is mainly at-

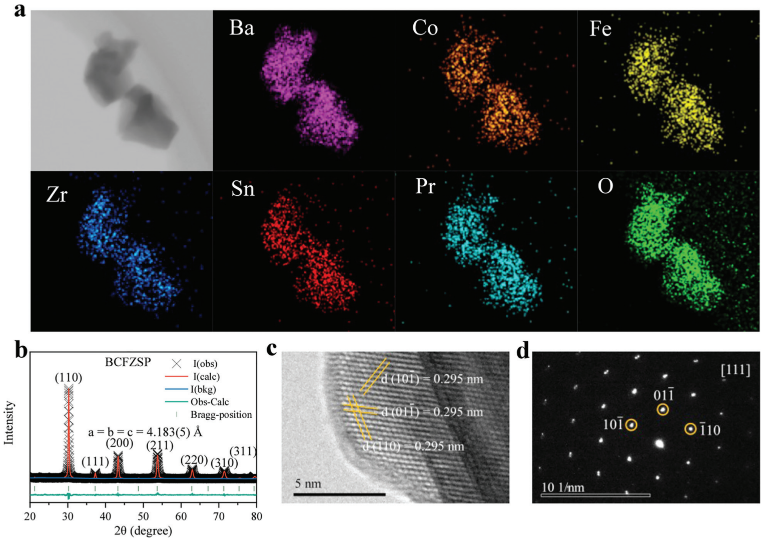

Fig. 1. Crystal structure of the high-entropy BCFZSP perovskite: (a) EDS maps of Ba, Co, Fe, Zr, Sn, Pr, and O. (b) Rietveld refinement room-temperature XRD pattern; (c) HR-TEM image; (d) SAED pattern along the [111] zone axis.

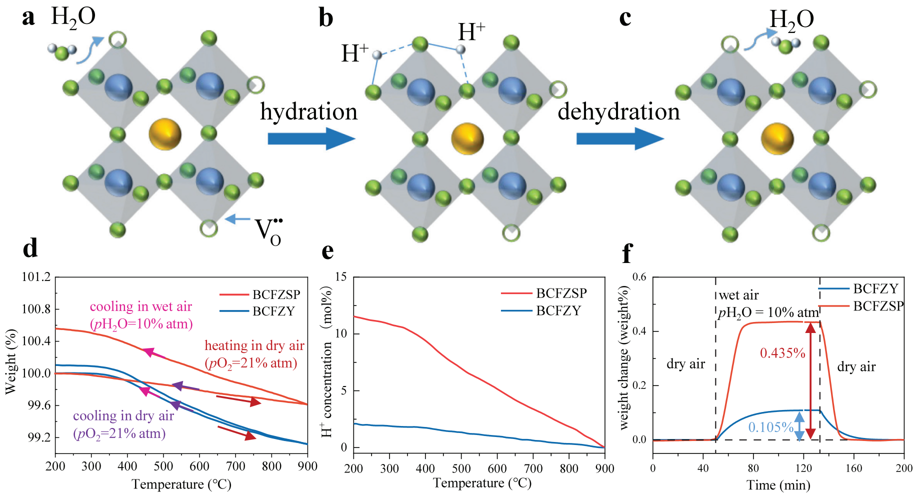

Fig. 2. Schematics of (a) H_2O adsorption from air to oxygen vacancies, (b) formation of proton defects, and (c) H_2O desorption from oxygen vacancies to air. (d) Cooling TG plots in dry and wet atmospheres. (e) Calculated proton concentrations in the BCFZSP and BCFZY samples. (f) Thermogravimetric relaxation curves based on rapid switching from dry to wet ($p(H_2O) = 10\%$ atm) condition.

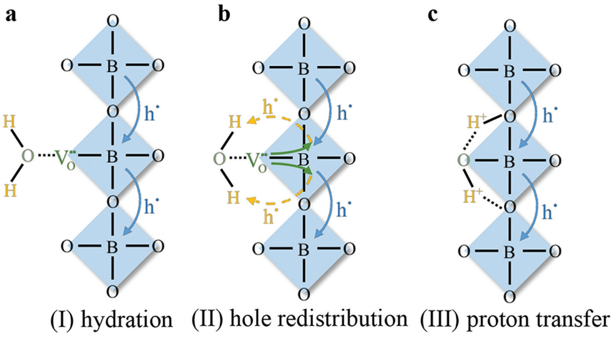

Fig. 3. Schematics of hole redistribution and proton migration as $p(H_2O)$ increases: (a) combination of water and oxygen vancy, (b) hole redistribution, (c) proton transfer.

tribute to hole concentration. During hydration, O from H_2O generates holes ($O + V_O^{\cdot\cdot} \longrightarrow O_O^{\times} + 2h^{\cdot}$) while H from H_2O consumes holes ($2H + 2h^{\cdot} \longrightarrow 2H^+$, Fig. 3b). Thus, the diffusion of O^{2-} increases hole concentration, while the transfer of H^+ decreases the hole concentration. Those two concurrent opposite influence on hole concentration results in nonmonotonic conductivity change. The initial drop of conductivity reveals the quicker diffusion of H^+ than that of O^{2-} in BCFZSP. As a contrast, the conductivity of BCFZY increases first and then decreases (Fig. 4c), suggesting a slower diffusion of H^+ than the O^{2-} in BCFZY. These results qualitatively demonstrate that BCFZSP manifests much more excellent proton mobility than the classic BCFZY material, showing great application potential in RPCC in light of the important effect of proton transfer on the electrode performance.

The comparison of Figs. 4a and c indicates that the electronic conductivity of BCFZSP is lower than that of BCFZY. Given that the electronic conduction is formed by hole jumping between the Co(Fe)–O–Co(Fe) bonds, the lower electronic conductivity of BCFZSP can be explained by its less Co/Fe composition ratio. Furthermore, parameters for quantifying ion conduction, including chemical diffusion coefficients of oxygen ions ($D_{O,chem}$)

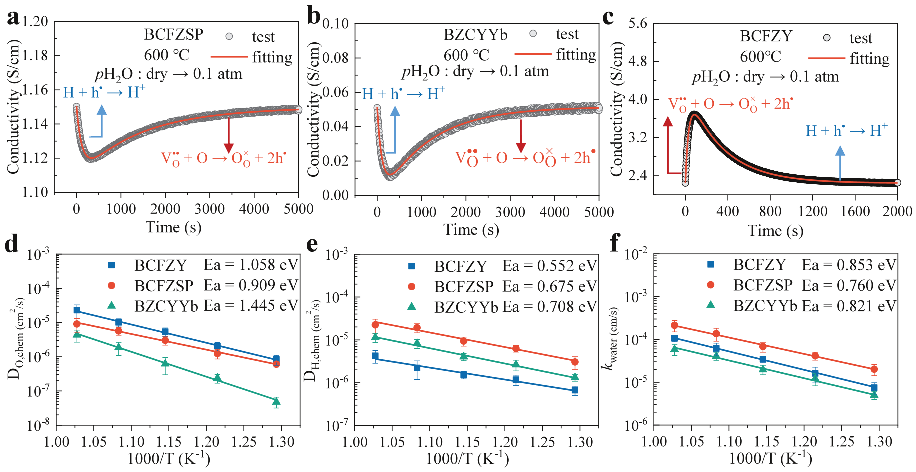

Fig. 4. ECR curves of (a) BCFZSP, (b) BZCYYb, and (c) BCFZY under $p(H_2O)$ switching from dry to 10% atm at 600 °C; Fitted (d) $D_{O,chem}$, (e) $D_{H,chem}$, and (f) k_{water} plots of the BCFZSP, BCFZY, and BZCYYb samples.

and protons ($D_{H,chem}$) and exchange coefficient of water (k_{water}), were calculated by fitting the ECR data with diffusion equations (Eqs. S4–S7) in Supporting information). Figs. 4d–f show the Arrhenius curves of $D_{O,chem}$, $D_{H,chem}$ and k_{water}, respectively. The E_a of $D_{O,chem}$ in BCFZSP was lower than that of BCFZY, revealing a lower energy barrier for oxygen-ion migration in BCFZSP. BCFZSP also presents excellent proton mobility and water exchange coefficient. For instance, from 500 °C to 700 °C, the $D_{H,chem}$ (3.05–22.37 × 10^{-6} cm^2/s) and k_{water} (2.01–21.29 × 10^{-5} cm/s) of BCFZSP are much higher than those of BCFZY ($D_{H,chem}$: 6.69–42.50 × 10^{-7} cm^2/s, k_{water}: 7.49–106.30 × 10^{-6} cm/s) and BZCYYb ($D_{H,chem}$: 1.31–11.36 × 10^{-6} cm^2/s, k_{water}: 4.89–58.61 × 10^{-6} cm/s).

The electrochemical impedance spectroscopy results display that BCFZSP shows the polarization resistance (R_p) of 0.448 Ω cm^2 (Fig. S3 in Supporting information), about half of that of BCFZY (0.932 Ω cm^2). It is also noted that the R_p and E_a values of BCFZSP decrease with increasing $p(H_2O)$, indicating the positive effect of proton transfer on extending the active sites of ORR and OER [20]. The performance of BCFZSP under actual cell operating conditions was evaluated in an anode-supported single cell composed of the NiO-BZCYYb anode, BZCYYb electrolyte (~8 µm) and BCFZSP electrode (Fig. 5a). In fuel-cell mode, the single cell displayed high peak power densities of 0.93, 0.79, 0.67, 0.48 and 0.33 W/cm^2 at 700 °C, 650 °C, 600 °C, 550 °C and 500 °C, respectively (Fig. 5b). These results are superior to BCFZY (Fig. S4 in Supporting information). Fig. 5c presents the current–voltage (*I–V*) curves in electrolysis mode at 500–700 °C with $pH_2O = 20\%$. At an applied voltage of 1.3 V, the current density reached 0.35, 0.61, 0.92, 1.20, and 1.76 A/cm^2 at 500 °C, 550 °C, 600 °C, 650 °C, and 700 °C, respectively. BCFZSP surpasses BCFZY in current density at each temperature (Fig. S5 in Supporting information) and dominates over most of those previously reported air electrodes (Table S3 in Supporting information). It can be also noted that hydrogen production rate in same current density decreased as temperature increased (Fig. 5d), indicating the lower Faraday efficiency of electrolysis at the high temperature (Fig. 5e). This result can be attribute to increased electron leakage on protonic electrolyte as temperature increased [21]. The energy efficiency at 600 °C in electrolysis mode (Fig. 5f) reached 68.76%, 63.68%, 62.14%, 58.65%, 55.32% and 53.34% at −0.75, −1, −1.25, −1.5, −1.75 and −2 A/cm^2, respectively.

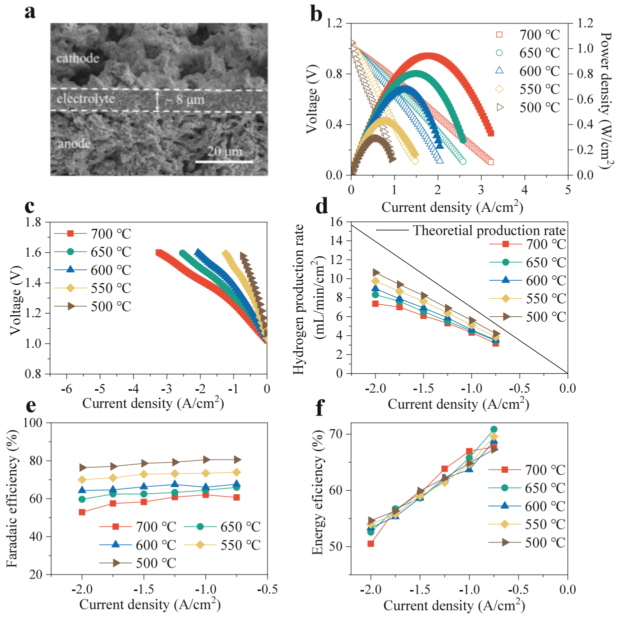

Fig. 5. (a) SEM image of an RPCC with the Ni-BZCYYb anode, BZCYYb electrolyte, and BCFZSP electrode. (b) Output performance in fuel-cell mode. (c) *I–V* curves measured in electrolysis mode. (d) Hydrogen production rates, (e) Faradaic efficiencies, and (f) energy efficiencies of current density in electrolysis mode.

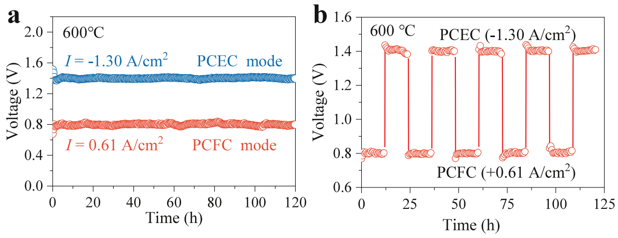

Fig. 6. (a) Stability tests in fuel-cell and electrolysis modes; (b) stability test during several cycles of switching between fuel-cell and electrolysis modes.

Long-term stability was confirmed under a constant current density of −1.3 A/cm^2 in electrolysis mode and 0.61 A/cm^2 in fuel-cell mode at 600 °C (Fig. 6a). Furthermore, stability cycling when switching between the fuel-cell and electrolysis modes was tested at 600 °C (Fig. 6b). Inappreciable performance degradation was observed throughout 5 reversible switching cycles (120 h). The excellent electrochemical stability suggests that high-entropy BCFZSP is a promising air electrode for RPCCs.

In summary, RPCCs electrode BCFZSP with cubic structure was successfully fabricated by a high-entropy design strategy, which had high electrochemical performance and stability. Compared with BCFZY, BCFZSP presented a higher proton diffusion coefficient. The BCFZSP electrode was successfully applied in RPCC. At 600 °C, the peak power density reached 0.68 W/cm^2 in fuel-cell mode. The current density reached −0.92 A/cm^2 at 1.3 V in electrolysis mode. More importantly, the stability remained 120 h of reversible switching operations between the fuel-cell and electrolysis modes. Overall, high-entropy perovskite oxide is a promising new platform for designing RPCCs electrodes.

Declaration of competing interest

The authors declare that they have no known competing financial interests or personal relationships that could have appeared to influence the work reported in this paper.

Acknowledgments

This work was financially supported by the National Natural Science Foundation of China (Nos. 22078022, 22178023, 22179007) and China Postdoctoral Science Foundation (No. 2021M690379). We also thank Analysis & Testing Center, Beijing Institute of Technology for providing XRD equipment.

Supplementary materials

Supplementary material associated with this article can be found, in the online version, at doi:10.1016/j.cclet.2022.107776.

References

[1] Y. Liu, Z. Yu, J. Chen, et al., Chin. Chem. Lett. 33 (2022) 1817–1830.
[2] A. Hauch, R. Kungas, P. Blennow, et al., Science 370 (2020) eaba6118.
[3] D. Ding, Y. Zhang, W. Wu, et al., Energy Environ. Sci. 11 (2018) 1710–1716.
[4] S. Choi, C.J. Kucharczyk, Y. Liang, et al., Nat. Energy 3 (2018) 202–210.
[5] Y. Niu, Y. Zhou, W. Zhang, et al., Adv. Energy Mater. 12 (2022) 2103783.
[6] G. Li, Y. Gou, R. Ren, et al., J. Power Sources 508 (2021) 230343.
[7] R. Ren, Z. Wang, X. Meng, et al., ACS Appl. Energy Mater. 3 (2020) 4914–4922.
[8] R. Ren, Z. Wang, C. Xu, et al., J. Mater. Chem. A 7 (2019) 18365–18372.
[9] Y. Zhou, E. Liu, Y. Chen, et al., ACS Energy Lett. 6 (2021) 1511–1520.
[10] M.Z. Liang, Y.J. Zhu, Y.F. Song, et al., Adv. Mater. 34 (2022) 2106379.
[11] Y. Niu, W. Huo, Y. Yu, et al., Chin. Chem. Lett. 33 (2022) 674–682.
[12] R. Ren, J. Sun, G. Wang, et al., Sep. Purif. Technol. 299 (2022) 121780.
[13] H. Zhang, K. Xu, F. He, et al., Adv. Energy Mater. 12 (2022) 2200761.
[14] X. Kuai, G. Yang, Y. Chen, et al., Adv. Energy Mater. 9 (2019) 1902384.
[15] N. Han, R. Ren, M. Ma, et al., Chin. Chem. Lett. 33 (2022) 2658–2662.
[16] C.M. Rost, E. Sachet, T. Borman, et al., Nat. Commun. 6 (2015) 8485.
[17] Z. Li, B. Guan, F. Xia, et al., ACS Appl. Mater. Interfaces 14 (2022) 24363–24373.
[18] Z.Y. Jin, J. Lyu, Y.L. Zhao, et al., Chem. Mater. 33 (2021) 1771–1780.
[19] T. Wang, H. Chen, Z.Z. Yang, et al., J. Am. Chem. Soc. 142 (2020) 4550–4554.
[20] Y.S. Song, Y.B. Chen, W. Wang, et al., Joule 3 (2019) 2842–2853.
[21] C. Duan, R. Kee, H. Zhu, et al., Nat. Energy 4 (2019) 230–240.